

# NUMERICAL SIMULATION ANALYSIS OF INFRARED RADIATION AND ELECTROMAGNETIC SCATTERING CHARACTERISTICS OF DIFFERENT MIXERS

Rui Wang<sup>1</sup>, Qingzhen Yang<sup>1</sup>, Saile Zhang<sup>1</sup> & Kai Du<sup>2</sup>

<sup>1</sup>School of Power and Energy, Northwestern Polytechnical University, Xi'an 710072, China

<sup>2</sup>Guiyang Aero-engine Research Institute, Guiyang 550081, China

## Abstract

In order to study the overall stealth performance of the exhaust system, three different mixers were presented to suppress infrared (IR) signature and reduce the system's radar cross section (RCS). The Reversed Monte-Carlo Method (RMCM) was used to calculate the infrared (IR) radiation characteristics, and the iterative physical optic approach (IPO) with equivalent edge currents method (EEC) was used to calculate the electromagnetic scattering characteristics of the electrically large nozzle. The results show that the lobed mixer has a lower IR radiation intensity within the detection angle of  $155^\circ \sim 175^\circ$ , which is 40% lower than that of the annular mixer and has a better IR suppression effect. The average RCS value of the nozzle with the lobed mixer is lower than that of the annular mixer, which is reduced by 50% in vertical polarization and 68.8% in horizontal polarization. After comprehensive evaluation and selection of various mixers, the lobed mixer is effective in terms of radar/infrared integrated stealth design.

**Keywords:** Lobed mixer, Infrared radiation, Radar cross section, Reverse monte carlo method, Iterative physical optics

## 1. Introduction

The new generation of stealthy fighters is the key development aircraft of the air forces in the future. With the continuous development of IR and radar detection equipment in modern warfare, the stealth characteristics of military aircraft will meet new challenges. The nozzle as the main component of the engine exhaust system can be a major contributor to total vehicle Radar Cross Section (RCS) due to its electrically large open-ended cavity properties. In addition, the high temperature components and the exhaust stream are also the main sources of IR radiation in the  $3\sim 5\mu\text{m}$  band[1]. Therefore, it's important to reduce the IR radiation and radar scattering from the exhaust system components.

The lobed mixer is applied to the exhaust system, which makes the internal high-temperature gas and external cold flow mixed, effectively reducing the IR radiation signal of the fighter. And the suitable mixer can attenuate the radar bypass echo, reduce the radar scattering area, and improve the backward electromagnetic stealth capability of the nozzle[2, 3, 4]. Regarding the IR suppression effect of lobed mixer mostly for the helicopter exhaust system, Zhang[5, 6], Shan[7], et al. analysed and experimentally verified the IR suppression effect of lobed mixer for the helicopter. Chen[8] et al. numerically studied the effect of the exit parameters of 2-D curved mixing duct on the aerodynamic and IR characteristics of the lobed infrared suppressor. Applying the lobed mixer to the exhaust system of the turbofan engine can give full play to its advantages in mixing compared with the traditional annular mixer, and reduce the IR radiation intensity of the exhaust system.

For the RCS calculation of the nozzle, the previous study is mostly concentrated on the nozzle shape. Li[9] carried out the RCS calculation and analysis for different outlet shapes of the s-shaped nozzle. Yang[10] compared and analysed the RCS of the axisymmetric and 2-D nozzle. And Gao[11] conducted a numerical study of the RCS for different aspect ratios of the 2-D nozzle outlet. Therefore,

there are few comparative analyses of the internal components of the nozzle. In this study, three various mixers including annular mixer, funnel-shaped mixer and lobed mixer, are carried out to analyse the IR and electromagnetic scattering characteristics.

## 2. Model

### 2.1 Geometric Model

A sketch of the axisymmetric 3D nozzle with inner and outer culvert, central cone, and mixer is designed as shown in Figure 1. Three different mixers are designed, namely annular mixer, funnel-shaped mixer, and lobed mixer respectively, whose 3D geometry is shown in Figure 1. To ensure the reliability of calculation results, other components of the exhaust system, referring to the central cone, nozzle wall, inlet, and outlet, etc., remain unchanged. Additionally, by adjusting the shapes of funnel-shaped and lobed mixer based on the annular mixer, the calculation models keep the same culvert ratio under the same internal and external inlet conditions.

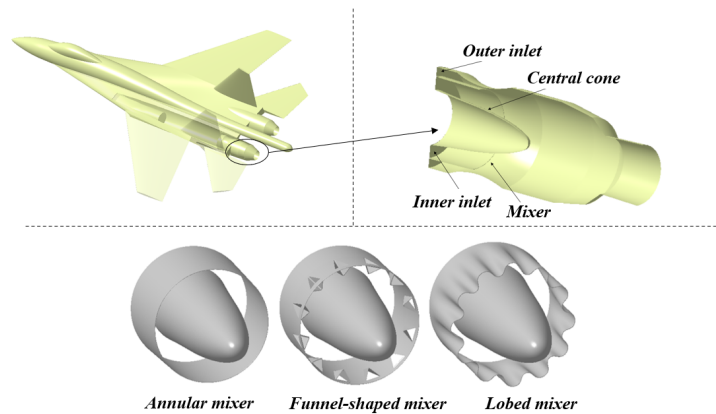


Figure 1 – Models of aircraft, exhaust system, and mixers.

### 2.2 Numerical Simulation Method of Flow Field

The hybrid mesh is employed for the half-mode meshing of the entire fighter model with various mixers, with about 6 million meshes, as demonstrated in Figure 2. And the height is 11km, the calculation condition is the high-altitude cruise state,  $Ma=0.8$ . Furthermore, the internal and external culverts' boundary conditions are the pressure-inlet, and the far-field boundary is pressure-far-field. The SST  $k - \omega$  model is used for turbulence model, the DO model is used for radiative heat transfer, and the WSGGM Gray Gas Weighted model is used to calculate the radiative properties of the gas mixture. And each equation's convergence accuracy is set at  $1 * 10^{-4}$ .

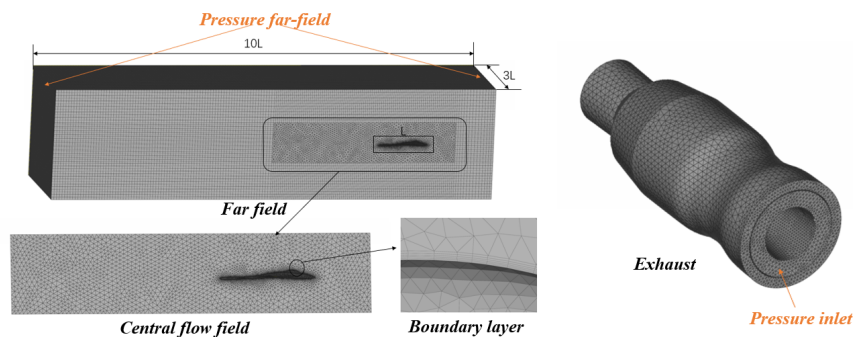


Figure 2 – Flow field establishment and mesh for model.

### 2.3 Observation field and model size

When calculating the infrared radiation characteristics, the calculation is carried out for the whole aircraft. The relevant observation field is set as shown in Figure 3. However, when calculating the

electromagnetic characteristics of different mixers, it is difficult to simulate the whole aircraft due to the limitation of the number of grids and the computational memory requirements, only the nozzle itself is calculated. Since the nozzle is axisymmetric, when calculating the electromagnetic scattering characteristics of the nozzle, the detectors are viewed from  $0^\circ$  to  $30^\circ$  on the pitch detection plane with an interval of  $1^\circ$ . The frequency of calculation is 10GHz, and the wavelength  $\lambda$  is 30mm.

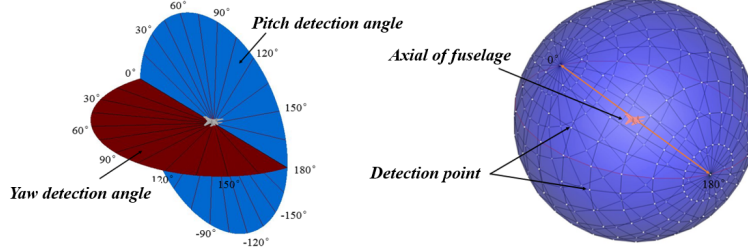


Figure 3 – Observation field setting for electromagnetic scattering and IR radiation.

### 3. Model Validation

#### 3.1 the Reverse Monte-Carlo Method

Reverse Monte Carlo Method (RMCM) is applied to simulate the IR radiation characteristics of the model. Because RMCM simulates the physical process without discretizing the spatial stereo angle of the incident plane[12, 13], it can easily deal with difficulties involving complex geometries and anisotropic scattering. When dealing with the radiation transmission problem in heterogeneous media, the calculation is only related to the radiation of the surface itself, avoiding the calculation of the effective radiation of the solid wall, so the number of rays can be greatly increased without increasing the processing cost, and the calculation accuracy can be improved. The spectral intensity observed from the detector can be obtained by:

$$I_\lambda = \frac{\Omega_{FOV} R^2}{\pi N} \sum_{i=1}^N E_{b\lambda}(i) \quad (1)$$

where  $E_{b\lambda}$  is the intensity of blackbody spectrum at the  $i_{th}$  random ray absorption point,  $\Omega_{FOV}$  is the field-of-view stereo angle of the detector, R is the detection distance, and N is the number of rays. The IR radiation properties of the high-temperature components of the nozzle can be obtained by solving the radiation transfer equation(RTE):

$$\frac{I(\mathbf{r}, \mathbf{s})}{ds} + (a + \sigma_s)I(\mathbf{r}, \mathbf{s}) = an^2 \frac{\sigma T^4}{\pi} + \frac{\sigma_s}{4\pi} \int_0^{4\pi} I(\mathbf{r}, \mathbf{s}') \Phi(\mathbf{s}, \mathbf{s}') d\Omega' \quad (2)$$

where  $\mathbf{r}$  is the position vector,  $\mathbf{s}$  is the direction vector, s is the length along the path,  $\sigma$  is the Stefan-boltzmann constant,  $\sigma_s$  is the scattering coefficient, a is the absorption coefficient,  $\mathbf{s}'$  is the scattering direction vector, n is the refractive index, T is the local temperature,  $\Phi$  is the scattering phase function, and  $\Omega'$  is the solid angle. Assuming that the fuel is completely burned in the engine combustion chamber, the RTE can be simplified to the following form:

$$\frac{L(\mathbf{r}, \mathbf{s})}{ds} + aL(\mathbf{r}, \mathbf{s}) = a \frac{\sigma T^4}{\pi} \quad (3)$$

Based on RMCM and ray tracing method, the radiation of the detector received could be determined as:

$$E = \sum_{i=1}^{N_B} \sum_{j=1}^N L_{\sigma}^n \cdot \cos\theta_j \cdot \Delta\Omega_j \cdot \Delta\sigma_i \cdot 100 \quad (4)$$

where E is the radiant illumination,  $N_B$  is the total number of wavebands, N is the total number of rays contributing to the measurement point,  $\theta_j$  is the angle between the center of the j-th solid angle and the surface normal of its measuring point, and  $\Delta\sigma_i$  is the width of the i-th wave band.

### 3.1.1 Model Validation

A disc is used as a numerical verification example to test the validity and precision of RMCM. The radius of disc is 1 meter, the emissivity is 1.0, and the surface temperature is 400K. Figure 4 shows the comparison between the numerical and theoretical results in 3-5  $\mu\text{m}$ . The curve demonstrates that the numerical solution of the RMCM method utilized in this study agrees well with the theoretical solution.

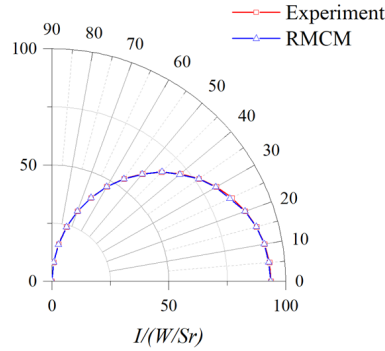


Figure 4 – Verification of infrared radiation calculation method.

### 3.2 the Iterative Physical Optic Approach

Iterative physical optic[14] (IPO) method is used to calculate the radar cross section (RCS) of the nozzle scattering field. Equivalent Edge Current (EEC) method is applied to simulate the diffraction effects at the nozzle edges. The IPO method is an iterative method based on physical optics (PO) that solves the integral equation of the cavity's magnetic field multiple scattering iteratively. IPO method only needs to divide 9 16 cells per square wavelength, which consumes less memory and has higher computational efficiency compared to method of moments (MOM) and other methods.

The nozzle is located behind the combustion chamber and turbine and other complex structures, only a small part of the electromagnetic wave can be propagated from the intake, thus the inlet of the nozzle can be simplified as a short circuit. As shown in Figure 5, the internal surface of the nozzle cavity is denoted as  $S_c$  and the virtual aperture surface at the nozzle exit is denoted as  $S_a$ . Since the radar is far from the target, the incident electromagnetic wave can be approximated as a uniform plane electromagnetic wave. According to the electromagnetic field equivalent principle, the equivalent electromagnetic current on the aperture surface  $S_a$  is

$$\begin{aligned} J_a^i(r_a) &= n_a \times H_a^i(r_a) \\ M_a^i(r_a) &= E_a^i(r_a) \times n_a \end{aligned} \quad (5)$$

where  $E_a^i(r_a)$ ,  $H_a^i(r_a)$  is obtained by the incident electric field and magnetic field,  $r_a$  is the positive vector of any point on the cavity aperture surface,  $n_a$  is the normal unit vector pointing into the cavity on the  $S_a$ .

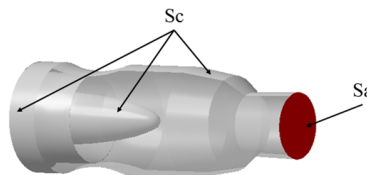


Figure 5 – Open-ended nozzle.

The magnetic field generated on the inner wall surface of the cavity can be obtained by Kirchhoffs

approximation:

$$H_0(r_c) = \int_{S_a} [J_a^i(r_a) \times \nabla G(r_c - r_a)] dS_a + \frac{1}{jkZ} \nabla \times \int_{S_a} [M_a^i(r_a) \times \nabla G(r_c - r_a)] dS_a \quad (6)$$

where  $Z$  is the free-space wave impedance,  $k$  is the free-space wave number,  $r_c$  is the position vector of any point on  $S_c$ , and  $G$  is the free space Green's function.

Before using the IPO method to calculate the equivalent electromagnetic flow, it is necessary to determine the masking relationship of the internal wall surface elements of the cavity. A detailed explanation can be obtained from Chen [15].

The current distribution on  $S_c$  is calculated iteratively by the magnetic field integral equation (MFIE):

$$J_N(r_c) = J_0(r_c) + 2n_c \times P.V. \int_{S_c} [J_{N-1}(r_c) \times \nabla G(r_c - r_c)] dS_c \quad (7)$$

where P.V. is the principal integral number,  $N$  is the number of iterations,  $\nabla$  is the Hamiltonian operator,  $r_c, r_c$  are the position vectors of the inter-irradiated points on the inner wall. Then, the scattering field is obtained on the aperture surface:

$$E^s(r_a) = \frac{1}{jkY} \nabla \times \int_{S_c} [J(r_c) \times \nabla G(r_a - r_c)] dS_c \quad (8)$$

$$H^s(r_a) = \int_{S_c} [J(r_c) \times \nabla G(r_a - r_c)] dS_c \quad (9)$$

where  $Y = 1/Z$ . Finally, using the field equivalence principle, the far-field scattering field  $E_s$  can be obtained from the equivalent electromagnetic current of the surface scattering field of the cavity.

### 3.2.1 Model Validation

The RCS calculation research was carried out on the angle inverter model provided in Reference [16] in order to verify the accuracy and reliability of the program, and the calculation results and experimental results in the literature were compared. The three edges  $I_{tri}$  that make up the top angle are all 5, as seen in Figure 6.

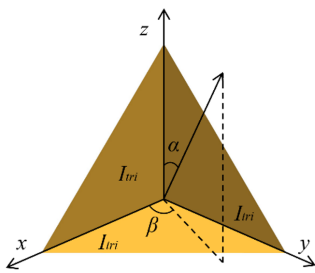


Figure 6 – Geometry of triangle trihedral corner. ( $\beta = 35^\circ$ )

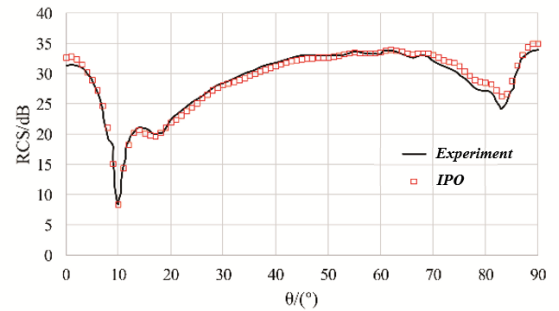


Figure 7 – Validation of the RCS algorithm.

Figure 7 is the RCS value of the model in Figure 6 when the side length is  $10\lambda$ . The calculated wavelengths and angles are in agreement with the above models. The comparison between the calculation results in this paper and the calculation results and experimental data in the literature is in the Figure 7.

## 4. Results and Discussion

### 4.1 Analysis of Flow Characteristics

The analysis was carried out using three different mixers. Figure 8 shows the dimensionless temperature distribution contours for three distinct mixer exhaust systems. The left side of the figure

represents the funnel-shaped mixer, and the temperature of nozzle tail's inner wall is higher than the others; and the right side represents the lobed nozzle, and the temperature is second; and the annular mixer is relatively the lowest.

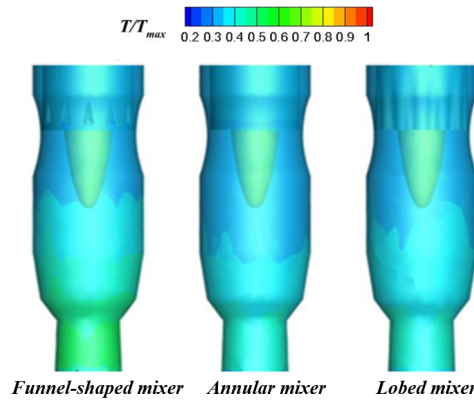


Figure 8 – Effects of mixers on the temperature distribution of the nozzle.

The exhaust system was sectioned at five various points. Figure 9 depicts the dimensionless temperature distribution of the exhaust system sections. The design of the mixer allows the external cold air flow to inject and squeeze the internal high-temperature gas so that the high-temperature gas diffuses outward, yet part of the external cold flow and the internal high-temperature gas mix directly. It results in the construction of daisy-petal-shaped temperature distribution in Figure 9. The difference is that funnel-shaped mixer's cold airflow striking the high-temperature gas is not as intense in the nozzle with the lobed mixer, therefore the temperature in the tail nozzle is likewise lower. However, the internal and external airflow mixing effect of the nozzle with the annular mixer is poor, making it difficult to transport high-temperature gas to the wall, resulting in a low temperature of the tail's inner wall. In conclusion, the lobed mixer has a greater mixing effect than the funnel-shaped mixer, while the annular mixer has the worst.

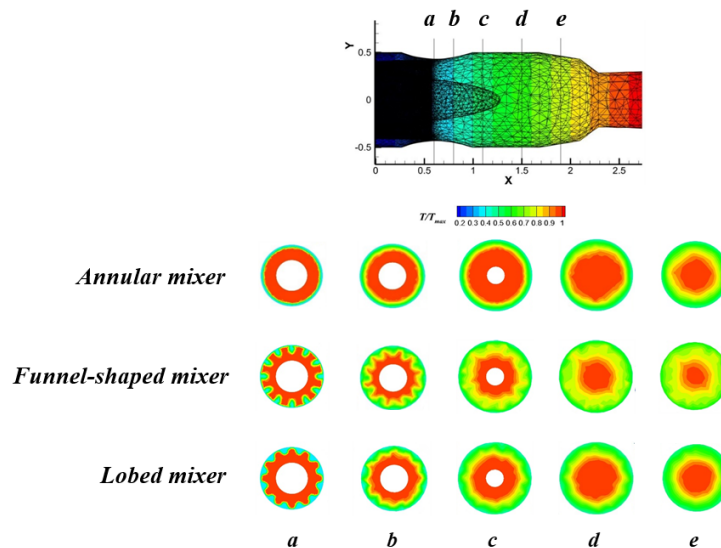


Figure 9 – Temperature distribution of the exhaust system sections.

$CO_2$ 's mass fraction distribution at the symmetry plane of nozzles with three different mixers are depicted in Figure 10, which have a similar distribution, with the highest  $CO_2$  mass fraction at the nozzle inlet, and decreasing along the axial direction. The  $CO_2$  mass fraction of the funnel-shaped mixer nozzle is the least after passing through the mixer, followed by the lobed mixer, and the annular mixer is the greatest, based on the position of the symmetry plane. The three temperature distribution laws are also comparable, as is the  $CO_2$  mass fraction distribution.

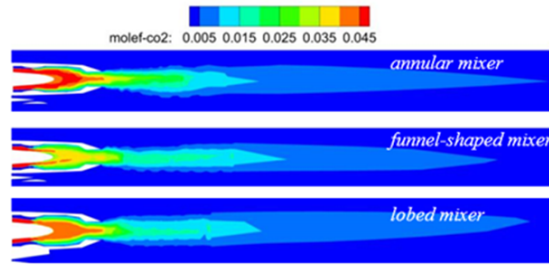


Figure 10 –  $CO_2$  mass fraction distribution of nozzles with three different mixers.

#### 4.2 Analysis of Infrared Radiation Characteristics

Based on the spatial distribution of temperature, pressure and atmosphere, RCMC is then applied to calculate the infrared radiation characteristics of the aircraft. Figure 11 shows the angular distribution curve of the dimensionless infrared radiation intensity on the nozzle with different mixers in the yaw detection surface. The nozzle with the funnel-shaped mixer has a higher infrared radiation intensity value, which corresponds to the temperature distribution law.

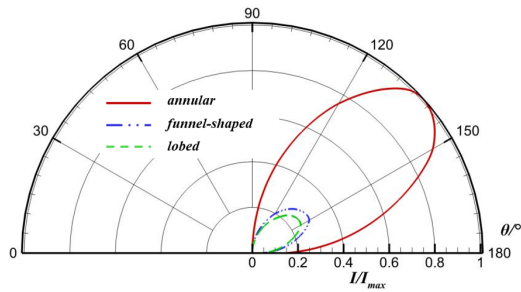


Figure 11 – The IR radiation characteristics of nozzle with different mixers.

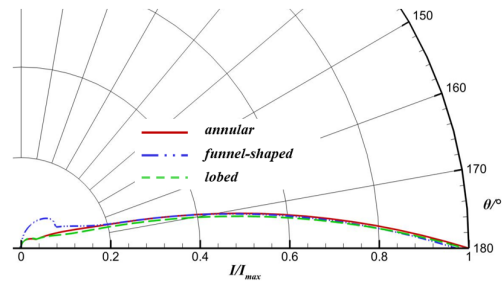


Figure 12 – The IR radiation intensity of fighters with different mixers in the yaw detection plane.

The angular distribution curve of the IR radiation intensity of fighters with varied mixer nozzles in the yaw detecting plane is depicted in Figure 12. At the backward  $180^\circ$  detection of three types of fighters with different mixers, the highest variation in infrared radiation value is found to be 3%. Furthermore, the IR radiation intensity of the jet with lobed mixer is lower than the other two types when the detection gradually decreases, in the region of  $155^\circ \sim 175^\circ$ . Because the alternating wave peak and dip diminish the high temperature area, the intensity of IR radiation is reduced. When the detection angle is less than  $165^\circ$ , the IR radiation of funnel-shaped mixer is the highest, almost 40% greater than the others. In summary, the jet with lobed mixer has a reduced IR radiation intensity and a higher infrared suppression effect.

#### 4.3 Analysis of Electromagnetic Scattering Characteristics

Because the axisymmetric nozzle with lobed mixer has outstanding infrared stealth qualities, this section compares the nozzle with annular mixer to the nozzle with lobed mixer to explore electromagnetic scattering properties in the X-band.

Figure 13 describes the RCS angular distribution curves in the X-band for two nozzles with variable mixers in the pitch detecting plane under vertical and horizontal polarization methods. The RCS of the nozzle with lobed mixer is smaller than the other in the detection angle of  $5^\circ \sim 26^\circ$ , under the RCS distribution in the vertical polarization mode. And the maximum value of both of those RCS appears inside the detection angle of  $0^\circ$ , and there is a local rising trend in the range of  $2^\circ \sim 10^\circ$ , and the overall RCS value displays a fluctuating decreasing pattern as the detection angle increases. This is due to the presence of a strong specular reflection area on the inlet of nozzle at the  $0^\circ$  detection angle, most of the radar waves are directly reflected back, generating a very strong echo source; at the  $2^\circ \sim 10^\circ$  detection angle, the inlet and other sections form an angular reflection with a strong

radar echo. The RCS value of the nozzle with lobed mixer is larger than the other under the horizontal polarization method, at 11°. This is due to the fact that an angle reflection area generated by the outlet and nozzle wall improves the radar echo.

The inductive current density distribution of annular mixer and lobed mixer under horizontal polarization observed from 11° is shown in Figure 14. The induction current density distribution is higher in the two-sided angle zone generated by the lobed mixer and inlet, and the radar wave can be incident via the valley to the outlet, resulting in a bigger RCS. However, the other's inductive current density is lower at the same location.

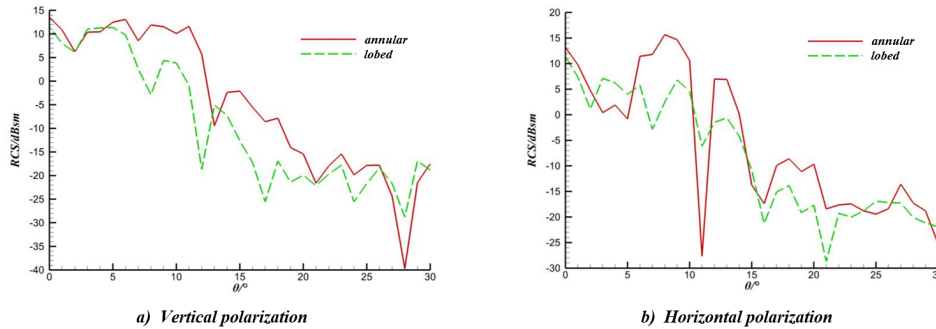


Figure 13 – Effects of different mixers on nozzle RCS.

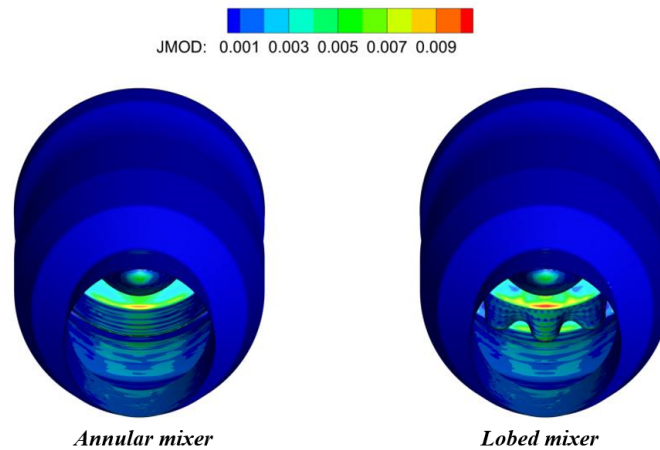


Figure 14 – Inductive current density of nozzles with different mixers at 11° under horizontal polarization.

Table 1 and Table 2 demonstrate the dimensionless RCS average values of the nozzle under the two polarization methods among the different detection angles in the pitch detection plane. The RCS average values of the nozzle with lobed mixer are lower than those with annular mixer, with a reduction of up to 50% in vertical polarization and 68.8% in horizontal polarization. To sum up, the lobed mixer has a good effect on improving radar stealth performance.

Table 1 – The dimensionless RCS average values of the nozzle

detection angle	vertical polarization		horizontal polarization	
	lobed mixer	annular mixer	lobed mixer	annular mixer
0° ~ 30°	0.2017	0.4041	0.1177	0.3769
0° ~ 20°	0.2974	0.5961	0.1734	0.5557
0° ~ 10°	0.5579	1.0000	0.3146	0.9828

## 5. Conclusions

In response to the overall stealth performance of the exhaust system of the advanced fighter, this study presents three types of mixers to improve the infrared and radar performance of the aircraft. By studying the infrared radiation and electromagnetic scattering characteristics of different mixers, the following conclusions can be drawn:

- The use of funnel-shaped mixer will form a daisy-petal-shaped high-temperature area to wash the inner wall of the nozzle, resulting in a high-temperature wall area. And compared with it, the wall temperature of the nozzle with lobed mixer is lower, and the mixing effect is better.
- In the 3~5 $\mu\text{m}$  band, the infrared radiation intensity of the nozzle with funnel-shaped mixer on the inner wall is larger than that of the annular mixer, and that of the lobed mixer is lower in the detection angle of 155°~175°, which is reduced by 40% relative to the annular one and has a better infrared suppression.
- At the detection angle of 0°, the RCS value is the maximum one among the detection angle. The average RCS value of the nozzle with lobed mixer is lower than that of annular mixer, which is reduced by a maximum of 50% in the vertical polarization, and 68.8% in the horizontal polarization.

## 6. Copyright Statement

The authors confirm that they, and/or their company or organization, hold copyright on all of the original material included in this paper. The authors also confirm that they have obtained permission, from the copyright holder of any third party material included in this paper, to publish it as part of their paper. The authors confirm that they give permission, or have obtained permission from the copyright holder of this paper, for the publication and distribution of this paper as part of the ICAS proceedings or as individual off-prints from the proceedings.

## References

- [1] Mahulikar, Shripad P and Sonawane, Hemant R and Rao, G Arvin. Infrared signature studies of aerospace vehicles. *Progress in aerospace sciences*, Vol. 43, pp 218-245, 2007.
- [2] Ponton, AJ. The use of concurrent engineering techniques in helicopter IR suppressor design. *AIAA-20051290*, 2005.
- [3] Mahulikar, SP and Prasad, HSS and Potnuru, SK. Infrared signature suppression of helicopter engine duct based on "conceal and camouflage". *Journal of Propulsion and Power*, Vol. 24, pp 613-618, 2008.
- [4] Yu, Simon CM and Yip, TH and Liu, CY. Mixing characteristics of forced mixers with scalloped lobes. *Journal of propulsion and power*, Vol. 13, pp 305-311, 1997.
- [5] Zhang, Jing-Zhou and Yong, Shan and Li, Li-Guo. Computation and validation of parameter effects on lobed mixer-ejector performances. *Chinese Journal of Aeronautics*, Vol. 18, pp 193-198, 2005.
- [6] Zhang, J and Shan, Yong and Li, L. Investigation on lobed nozzle mixer-ejector infrared suppressor for helicopter exhaust system. *ACTA AERONAUTICA ET ASTRONAUTICA SINICA-SERIES A AND B-*, Vol. 28, pp 32, 2007.
- [7] Shan, Yong and Zhang, Jingzhou and Li, Ligu. Numerical calculation and experimental verification for the infrared radiation characteristics of helicopter infrared radiation suppressor. *JOURNAL OF INFRARED AND MILLIMETER WAVES-CHINESE EDITION-* Vol. 25, pp 95, 2006.
- [8] Geng, Chen and Xiaoming, Tan and Yong, Shan and Jingzhou, Zhang. Impacts of two-dimensional curved mixing duct exit geometric parameters on flow dynamics and infrared radiation characteristics for IR suppressor. *Infrared and Laser Engineering*, Vol. 44, pp 1704-1711, 2015.
- [9] Li, YF and Yang, QZH and Li, Xiang and HUAN, Xia. RCS characteristic of S-shaped nozzle with different outlet shapes. *Journal of Aerospace Power*, Vol. 28, pp 2671-2677, 2013.
- [10] Yang, Tao and Yang, Qing-Zhen and Li, Yue-Feng. Numerical simulation of RCS for axisymmetric nozzles and symmetrical two-dimensional nozzle. *Journal of Aerospace Power*, Vol. 26, pp1819-1823, 2011.
- [11] GAO, Xiang and YANG, Qing-zhen and MU, Hong-rui and GUO, Xiao. Numerical simulation of radar scattering characteristics for 2-D nozzles with different aspect ratios. *Journal of Propulsion Technology*, 2014.
- [12] Wang, K. Prediction of rocket plume radiative heating using backward Monte-Carlo method. *31st Aerospace Sciences Meeting*, pp 137, 1993.

- [13] HUANG, Wei and JI, Hong-hu and SI, Ren and CHEN, Jun. Infrared characteristics calculating of turbofan engine exhaust system. *Journal of Propulsion Technology*, Vol. 31, pp 745-750, 2010.
- [14] Obelleiro-Basteiro, Fernando and Rodriguez, J Luis and Burkholder, Robert J. An iterative physical optics approach for analyzing the electromagnetic scattering by large open-ended cavities. *IEEE Transactions on antennas and propagation*, Vol. 43, pp 356-361, 1995.
- [15] Chen, Li-Hai and Yang, Qing-Zhen and Chen, Ling-Ling and Cui, Jin-Hui. Numerical simulation of RCS for 2-D convergent nozzle with different trailing edges. *Journal of Aerospace Power*, Vol. 27, pp 513-520, 2012.
- [16] Polycarpou, Anastasis C and Balanis, Constantine A and Birtcher, Craig R. Radar cross section of trihedral corner reflectors using PO and MEC. *Annales des télécommunications*, Vol. 50, pp 510-516, 1995.